Technical University of Denmark

DTU

Geometric calibration of ERS satellite SAR images

Mohr, Johan Jacob; Madsen, Søren Nørvang

DTU Library
Technical Information Center of Denmark

Geometric Calibration of ERS Satellite SAR Images

Johan Jacob Mohr and Søren Nørvang Madsen, *Member, IEEE*

Abstract—**Geometric calibration of the European Remote Sensing (ERS) Satellite synthetic aperture radar (SAR) slant range images is important in relation to mapping areas without ground reference points and also in relation to automated processing. The relevant SAR system parameters are discussed and calibrated by using the European Space Agency (ESA) transponders at Flevoland. The resulting accuracy of the slant range images corresponds to 10 m horizontally on the ground. The results are verified by using runway intersections and corner reflectors surveyed with differential GPS techniques. Based on a seven-year ERS-1 and a four-year ERS-2 time series, the long term stability is found to be sufficient to allow a single calibration covering the entire mission period. A descending and an ascending orbit tandem pair of the ESA calibration site on Flevoland, suitable for calibration of ERS SAR processors, is described to allow other researchers to geometrically calibrate their processing systems.**

Index Terms—**European Remote Sensing (ERS) satellite, geolocation, geometric calibration, synthetic aperture radar (SAR), SAR interferometry.**

I. INTRODUCTION

A MAJOR achievement of European Remote Sensing (ERS) Satellite ERS-1/2 has been the accurate radiometrically calibrated SAR imagery, e.g., [1], [2]. However, the most spectacular success of ERS-1/2 is interferometry, which is geometric in character, [3]–[6].

In this paper, we describe our attempts to calibrate ERS-1/2 geometrically. Specifically, we discuss the following:

1) relevant ERS system parameters and how they are derived;
2) our approach to calibrate a satellite SAR sensor geometrically by using ground control points of limited horizontal accuracy;
3) calibration of the key parameters;
4) verification of the derived parameters;
5) stability of the derived parameters over the ERS-1/2 lifetime;
6) a standard calibration data set for ERS-1/2.

The information provided in the paper relates to the ERS-1/2 system. We used a Range-Doppler SAR processor designed for airborne as well as satellite data [7], but the results would also apply to SAR imagery focused with proper implementations of other algorithms, e.g., the wave-number or the chirp scaling algorithms, [8].

II. SAR GEOCODING

A multitude of scientific applications of satellite interferometric SAR data has evolved over the last few years. One of the challenges in the coming years is to bring the techniques to a level where, for example, regional or continental scale digital elevation models and displacement maps can be generated on an operational basis. This is important not only for commercial exploitation of satellite interferometric SAR data but also for many government and scientific applications.

Today, one of the key limitations in many processing systems is the need for manual identification of ground control points (GCPs). For large area mapping, automatic use of GCPs is obviously an advantage, but also in many areas, GCPs are very difficult or impossible to identify in the SAR images.

For geometric calibration, we use the fact that the SAR image in the slant range projection can be characterized by the slant range and the processing squint angle (Doppler) [9]. Provided that the acquisition geometry (the state-vectors) is known with sufficient accuracy, the mapping into the slant-range geometry of any given point with known geographical coordinates can be calculated.

This mapping from the three-dimensional (3-D) Earth-surface to two-dimensional (2-D) radar coordinates depends on radar system parameters only and is not image dependent. In the following, we show that a dead-reckoning approach supports mapping with a 10 m ground accuracy with ERS-1/2 data. This is the subject of the present paper.

The opposite mapping from radar coordinates to 3-D map coordinates requires a third coordinate, which can be obtained by using interferometric SAR. The accuracy of the third coordinate, the cross-range component, depends on the unwrapped (absolute) interferometric phase, which depends strongly on the scene and on the acquisition conditions (baseline, atmosphere, etc.). Therefore, it is much more difficult to quantify the final geolocation accuracy for interferometric SAR products. This mapping is not the subject of the present paper.

III. REQUIRED PARAMETERS

When interferograms are processed directly from raw data, only a few parameters are required. Determination of the geometry of the focused single look complex (SLC) SAR images requires knowledge of

- platform state vectors;
- time of reception for each pulse;
- slant range offset (corrected for internal delay in the radar);
- reference squint angle

in conjunction with other processing parameters, e.g., processing window offset. The SAR focusing additionally requires:

- carrier frequency f_c;
- sampling frequency f_s;
- knowledge of pulse encoding, e.g., chirp length, T_c, and bandwidth B_c.

IV. ERS PRECISION ORBIT DATA

For most ERS-1 and ERS-2 SAR acquisitions, precision orbit (PRC) data are available from the German Processing and Archiving Facility (D-PAF), Oberpfaffenhofen, Germany. The data format is excellently documented in [10]. The definition of different time scales and coordinate systems and conversions between the different datums is given in [11]. In particular, it should be noted that a transformation is given such that the orbit data provided in ITRF94 can be converted to WGS-84. The accuracy of the data are on the order of 10 cm to 30 cm for the satellite positions [12].

In cases where no PRC data are available, the D-PAF provides preliminary orbit (PRL) data. Finally, the leader file includes state-vectors with an accuracy better than 10 m, [13], [14]. This is sufficient for geolocation of data.

V. RAW ERS DATA PREPARATION

The raw data file(s) needs preprocessing before SAR focusing in order to

- correct for missing lines, by use of the image format counter (IFC);
- align data to correct for sampling window start time (SWST) changes, i.e., changes in slant range offset during the image acquisition;
- estimate the time of first line, i.e., the ICU (Instrument Control Unit) binary time of first line.

A. Missing Line Cleaning

Missing lines in the raw data cause an azimuth shift of the images, which in turn causes an easily observed degradation of interferograms. Furthermore, uncompensated missing lines cause along track shifts degrading the absolute geolocation accuracy. Missing lines can be corrected by adding dummy lines to the raw data. We use lines having an average of the nominal DC value, $(I, Q) = (15.5, 15.5)$, but that choice is not critical.

Typically, a standard ERS frame with nominally 28 000 raw lines has from zero and up to a few missing lines. However, near the borders of station coverage, the number of missing lines can increase dramatically. This suggests that missing lines are introduced by the data down-link chain. Our confidence in this assumption is strengthened by the fact that we have not observed missing line effects in data corrected by use of the IFC. The IFC is a part of the auxiliary information, attached to the raw data lines in the radar [15]. The IFC increments by one for each raw data line.

The correction for missing lines is not straightforward since the IFC is subject to bit errors. It is our experience that robustness of the algorithm is important. The selected algorithm is described in Appendix A

Merging of adjacent frames become very simple, if performed in a separate step after the cleaning. In this case, the cleaned IFC values, common in the overlap region, can directly be used as line identifiers.

B. SWST Cleaning

The integer sampling window start time (SWST) number determines the time offset between pulse transmission and sampling of radar echoes in units of $4T_s$, where T_s is the A/D sampling interval. To accommodate satellite altitude variations, the SWST is changed every 400 km along track, based on a look-up table [15]. The SWST values are available in each line of the raw data. It is our experience that the SWST is changed only in steps of 22 units. The relation between the SWST number and the slant range offset in seconds is given in Section VI.

It is convenient to align data according to the SWST and clean the SWST values after correction for missing lines and after merging of adjacent frames. It is noted that an uncorrected SWST bit error in one line only causes one line to be shifted by an erroneous amount, in effect replacing good data with noise. Due to the SAR focusing, this causes only a minor degradation of the image quality. The selected algorithm for SWST cleaning is detailed in Appendix A.

C. ICU Estimation

The satellite binary master clock is located in the On-Board Computer (OBC), [16]. It is used for datation of all events in the satellite including datation of raw radar data managed by the instrument control unit (ICU). The ICU binary clock values are available in each line of the raw data. A step by one corresponds to $1/256$ second. The value is updated every fourth raw data line. A method for ERS-1/2 users to convert an ICU value to coordinated universal time (UTC) is given in Section IV.

The relative accuracy of the ICU clock has been assessed using a mixture of ERS-1 and ERS-2 data. For eight data sets we extrapolated corresponding values of the ICU counter and UTC by 35 days and compared with the values provided in data acquired 35 days later. We find a relative accuracy on the order of $2 \cdot 10^{-7}$, which demonstrates the importance of frequent correlation of the ICU clock and UTC as performed by ESA via the Kiruna Station, [17].

One unit of the ICU corresponds to approximately 6.6 radar pulses. Thus, the third pulse after an ICU update may have a timing uncertainties of up to 9.6 pulses. This corresponds to 40 m along track and is not sufficient for precision geolocation. Therefore, a linear relation between raw data line numbers n_{raw}, and the ICU values is established. The linear relation is used to get an equivalent ICU (a floating point number) of the first raw data line, see Appendix A.

VI. RADAR PARAMETER SUMMARY

In this section, we summarize the extraction of SAR parameters from the leader file and the raw data file of the standard ERS.SAR.RAW product. The parameters used must support a geometric calibration scheme that is globally valid. The method is based on documentation from ESA, [15], [18], [19], processing experiments, and assumptions on implementation and stability of the ERS radar system. Details are found in Appendix B.

TABLE I
THE FOUR UPPER PARAMETERS CONSTITUTE THE CORE OF GEOMETRIC CALIBRATION. THE KEY PARAMETER IS THE VALUE OF THE SAMPLING INTERVAL
$T_s = 1/f_s$. THE BINARY SWST AND PRI ARE A PART OF THE HEADER DATA FOR EACH RADAR PULSE. THE SATELLITE BINARY TIME ICU$_b$ AND SATELLITE
CLOCK TIME ICU$_t$ ARE PROVIDED BY ESA IN AN AUXILIARY DATA FILE. WE USE THE CONSTANT VALUE 1/256 s FOR ICU$_\Delta$. THE CONSTANTS $t_{0,s} = 0$ s FOR
ERS-1 AND $t_{0,s} = -0.025\ \mu$s FOR ERS-2 EXPRESS A DELAY DIFFERENCE ESTIMATED BY USING TANDEM DATA (SEE SECTION VII). THE CALIBRATION
CONSTANTS DERIVED FROM OUR FLEVOLAND DATA ARE $t_{0,b} = 6.622\ \mu$s AND $t_{l,b} = 1.25$ ms; SEE SECTION IX

ERS-1/2 Radar Parameter Summary			
Parameter	Expression	Unit	Calibration
Range offset	$t_0 = 9T_p + \mathrm{SWST} \cdot 4T_s - t_{0,b} + t_{0,s}$	s	$t_{0,b}, t_{0,s}$
Sampling frequence	$f_s = 18.962\,468$	MHz	
Time of first line	$t_l = (t_{l,0} - \mathrm{ICU}_b) \cdot \mathrm{ICU}_\Delta + \mathrm{ICU}_t + t_{l,b}$	s	$t_{l,b}$
Pulse interval	$T_p = 4T_s(\mathrm{PRI} + 2)$	s	
Carrier frequency	$f_c = 5.300$	GHz	
Chirp length	$T_c = 37.12$	μs	
Chirp bandwidth	$B_c = 15.508\,29$	MHz	

The slant range offset, the range sampling spacing, the pulse repetition interval, and the carrier frequency are all based on a temperature controlled ultrastable oscillator that produces an output at nominally 61.6279 MHz (personal communication, R. Gelsthorpe, ESA/ESTEC). This frequency is doubled to the IF frequency of 123.2558 MHz, which is further multiplied by 42 to 5176.7436 MHz for use in the up/down-converters. The 123.2558 MHz signal is also divided by 13 and multiplied by 2 to yield the A/D sampling frequency, and this is in turn divided by 4 to provide a signal for the adjustable counters which controls the sampling window offset and the pulse repetition interval.

The parameters are summarized in Table I, where the A/D sampling frequency f_s is used as the basic parameter. We used the value of f_s provided by the D-PAF, which is insignificantly different from the value that can be derived from the reference oscillator frequency given above, see Appendix B. Our calibration experiments confirm the value of the sampling frequency and that it can be considered constant over time.

The SWST in units of $4T_s$ determines the slant range offset, for the pulse echoes which are received slightly more than nine pulse repetitions intervals after transmission. The calibration constants are provided in Table I. However, it is recommended to calibrate each SAR processor individually for $t_{0,b}$ and $t_{0,s}$ since different approaches for pulse compression may result in different positions of the compressed peak.

The pulse repetition interval T_p is calculated from the integer PRI value, which is in units of $4T_s$.

The time of first line is based on the estimated (floating point) binary time of first line $t_{l,0}$, which we derive from the integer ICU values of many lines. The binary time is converted to UTC by using information provided by ESA in the leader file.

Exact knowledge of the pulse parameters f_c, T_c, and B_c are not critical as long as they are kept constant in the processing. Changing the values may change the position of the compressed radar echoes.

VII. RELATIVE ACCURACY OF TANDEM PHASE DATA

In this section, we assess how well ERS-1 and ERS-2 Tandem data align when processed with the above parameters before cal-

ibration. We used the nominal value $t_{0,b} = 6.265\ \mu$s for the slant range offset bias, $t_{l,b} = 0$ s for the along track bias, and assumed identical delays ($t_{0,s} = 0$ s) in the ERS-1 and ERS-2 radars. The accuracy is a lower limit on the absolute accuracy of the mapping between geographical and radar coordinates, as common mode errors both static and varying with time add additional uncertainties. Sections IX–XI demonstrate that the common mode errors can be calibrated out, and Section XII shows that drift is insignificant.

It is our experience that even 2000 km long strips can be aligned sufficiently well for generation of interferograms by the use of a constant shift in range and azimuth. For optimal coherence, a nonlinear resampling could additionally be applied to accommodate (and estimate) excessive differences in surface motion, e.g., near-earthquake faults or fast moving ice, or to compensate for image distortions caused by ionospheric or possibly atmospheric distortions.

The alignment of ERS-1 and ERS-2 data in range and azimuth is investigated by using a mixture of ascending and descending orbit tandem pairs from Greenland (ten pairs), Aalborg, Denmark, (three pairs), and Flevoland, the Netherlands, (eight pairs). In each pair, the shifts are estimated by cross correlating 512 patches of 128 samples $\times$ 128 samples.

The estimated shifts in meters are shown in Fig. 1. Since both the uncertainty of the ERS-1 image and the ERS-2 image contribute to the observed shift, the root mean square (rms) uncertainty of the individual images is $1/\sqrt{2}$ of the rms of the combined shifts. In range, the mean difference is -3.8 m with an rms uncertainty of 1.1 m. We interpret that as a $t_{0,s} \approx -0.025$ μs differential delay for the ERS-2 radar. Excluding the two outliers (which are easily detectable in the processing), the azimuth uncertainty is 4.9 m, whereas 10.8 m is found if all data are included. Ignoring the two outliers, the results are in good agreement with experiences at the German Aerospace Center (DLR), Oberpfaffenhofen, Germany [20].

VIII. TRANSPONDERS

ESA has three transponders permanently deployed in Flevoland primarily for radiometric calibration of ERS images,
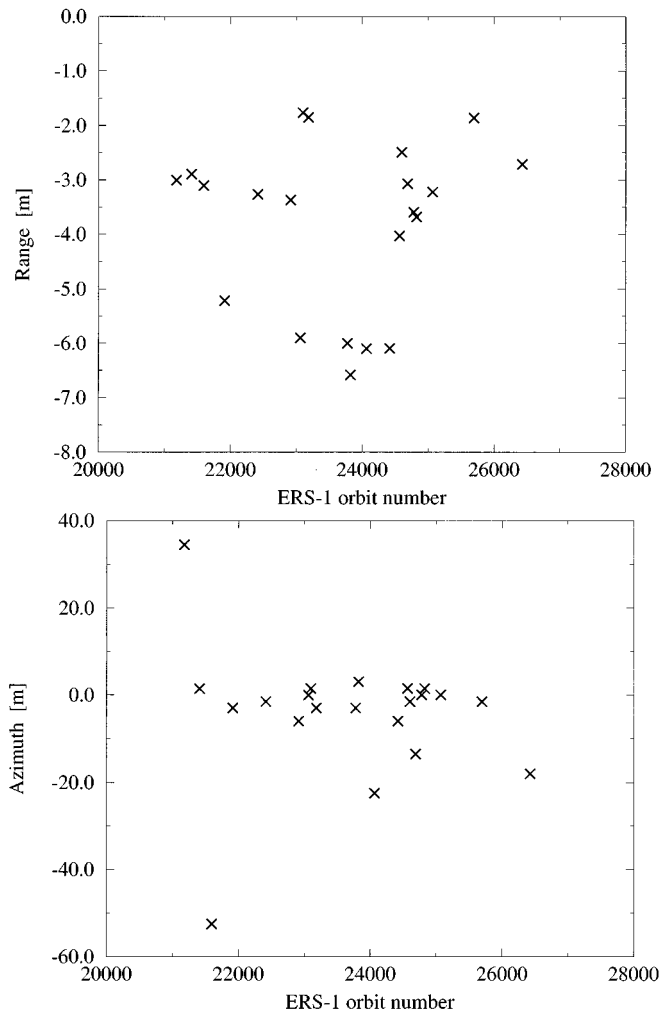
Fig. 1.   Estimated (a) range and (b) azimuth shifts (in meters) required to align 21 Tandem pairs. The two azimuth outliers are from pairs with ERS-1 orbits 21 181 and 21 596 from the initial part of the Tandem period.

TABLE II
WGS-84 TRANSPONDER POSITIONS (ϕ_0, λ_0) (IN DECIMAL DEGREES) AND TRANSPONDER DELAYS Δ_t (IN μs) AS PROVIDED BY ESA. ELLIPSOIDAL HEIGHTS h_M (IN METERS) AS FOUND FROM A MAP CORRECTED WITH A GEOID HEIGHT OF 43.6 M, AND AN ANTENNA HEIGHT OF 0.85 M. (ϕ_E, λ_E) ARE THE POSITIONS ESTIMATED FROM ERS DATA, AND (Δ_n, Δ_e) THE DIFFERENCES (IN METERS) IN THE NORTH AND EAST DIRECTIONS

	Flevoland transponders		
	T1	T2	T3
ϕ_0	52.366 4458	52.457 9114	52.554 9572
λ_0	5.152 2219	5.527 5536	5.668 9317
h_M	41.4	40.2	40.4
Δ_t	1.536	1.552	1.545
ϕ_E	52.366 4799	52.457 9151	52.554 9575
λ_E	5.152 0943	5.527 5521	5.668 9498
Δ_n	−3.8	−0.4	−0.0
Δ_e	8.7	0.1	−1.2

IX. CALIBRATION (FLEVOLAND)

Four ascending and four descending orbit tandem pairs covering Flevoland were used for calibrating our processing chain for a constant slant range bias $t_{0,b}$ and a constant azimuth bias $t_{l,b}$.

Due to the uncertainties in the GPS measurements, it was decided to estimate the horizontal transponder positions from the ERS data. This is possible because both ascending and descending orbit acquisitions are available. The transponder heights and the transponder delays, though, cannot be separated from a slant range bias. Therefore, Δ_t and h_M are used directly from Table II.

The ascending and descending orbit tracks are assumed having directions $-\psi$ and $180° + \psi$, respectively, where ψ is the direction relative to north, defined in a clockwise sense (meaning east is $+90°$). With an angle of incidence θ, the projections of the ascending and descending line-of-sight unit vectors $\hat{n}_a$, $\hat{n}_d$ on the $\hat{e}$, and $\hat{n}$ unit vectors in a Cartesian east, north, and up system become

$$\hat{n}_a \cdot \hat{e} = -\hat{n}_d \cdot \hat{e} = \cos \psi \sin \theta$$
$$\hat{n}_a \cdot \hat{n} = \hat{n}_d \cdot \hat{n} = \sin \psi \sin \theta.$$

The corresponding projections of the along track unit vectors $\hat{t}_a$ and $\hat{t}_d$ become

$$\hat{t}_a \cdot \hat{e} = \hat{t}_d \cdot \hat{e} = -\sin \psi$$
$$\hat{t}_a \cdot \hat{n} = -\hat{t}_d \cdot \hat{n} = \cos \psi.$$

The method is as follows. For each Tandem pair, two SLCs are formed, the relative shifts in range and azimuth are found, the error in the alignment is distributed equally between the ERS-1 and the ERS-2 images, the SLCs are reprocessed, and an interferogram is formed. Now a linear estimation problem can be set up. The observables are the difference between the observed and the predicted slant range, and azimuth positions of each of the transponders. The unknown parameters are the slant range bias and the azimuth timing bias (both assumed common for

[21], [22]. The transponders are controlled by lookup tables such that they are powered up and positioned to point to the ERS satellites on each overpass, both ascending and descending. However, during some overpasses, some or all transponders are not operated. In [1], an extensive investigation of radiometric calibration is given. In our study, those data have been used to identify orbit numbers with transponder activity.

A straightforward approach to geometric calibration requires knowledge of the transponder delays and the transponder positions, see Table II. The position measurements were carried out in 1991 using GPS and may be erroneous by tens of meters (personal communication, ERS Helpdesk). Therefore, the horizontal positions (ϕ_0, λ_0) are used as nominal positions only and refined during the calibration. The horizontal position of the transponders estimated from ERS data, though, differs by less than 10 m from the GPS measurements. The vertical positions h_M are found from a map [23]. A geoid correction of 43.6 m with an estimated accuracy of ± 0.5 m and an antenna height of 0.85 m above terrain were used [personal communication, R. Forsberg and H. Jackson].

the ascending and the descending orbit images) and an east and a north position error for each of the transponders. To improve the precision, the transponder positions are found in the SLCs, not in the interferograms.

The estimation results are shown in Table III for three estimations. In iteration 0, $t_{0,b} = 6.265$ μs and $t_{l,b} = 0$ s and the nominal (ESA) transponder positions rounded to three decimals are used. The rounding potentially introduces up to a 56 m error. The estimated slant range bias using our SAR processor is found to be $\Delta_r = 53.67$ m, corresponding to $t_{0,b} = 6.622$ μs. The estimated along track bias is found to be $\Delta_s = -9.9$ m, corresponding to $t_{l,b} = 1.25$ ms. Iteration 1 serves as verification. Here, the predicted positions are based on those derived from iteration 0. In the last column in Table III, the nominal transponder positions have been used, and only the slant range and the azimuth biases estimated. The standard deviations of the residuals have been divided into two components. The variations from interferogram to interferogram, $\sigma_{r,\mu}$ and $\sigma_{a,\mu}$ represent the uncertainties in range offset and azimuth timing. The estimation noise $\sigma_{r,n}$ and $\sigma_{a,n}$, assumed common for all interferograms, describes the consistency of the transponder measurements in one SLC image.

Table III shows a 0.4 m rms error in the slant range direction, corresponding to 1 m on ground, and a 5.7 m rms error in azimuth. This demonstrates an excellent stability of the ERS radar system.

The selected approach has the drawback that a scaling error in the slant range direction cannot be identified. This implies that a possible slant range stretch or shrink will be interpreted as position errors in the east-west direction. A validation using passive targets with known positions, distributed in range, does not have this drawback (see Section XI). A closer look at the positions and errors in Table II shows that the deviations between the positions provided by ESA and the estimated ones could be interpreted as a stretch in slant range. However, the sign is different from what is expected if the commonly cited value $f_s = 18.96$ MHz of the sampling frequency is correct rather than the one used.

X. VALIDATION (AALBORG)

Three descending tandem pairs covering Aalborg Airport, Denmark, have been used for validation. It is difficult to identify points with known geographical coordinates in ERS images. Here, the intersections of runways at Aalborg Airport have been used. The geographical coordinates and the heights are found from a map [24]. The SAR image coordinates are found as the intersection of the center lines drawn on the runways (see Fig. 2).

The results for the five points used are shown in Table IV. The mean slant range error for the three pairs is 1.4 m, corresponding to 3.5 m on the ground. The mean azimuth error is -21.8 m. However, it is also seen that a major part of this azimuth error originates from the pair I1, comprising ERS-1 orbit 21 596, from the initial phase of the tandem period, where also ERS-1 to ERS-2 consistency for some reason is degraded (see Fig. 1). Excluding that interferogram, the mean slant range error

TABLE III
Δ_r AND Δ_s (IN METERS) ARE THE ESTIMATED RANGE AND AZIMUTH BIASES FOUND USING OUR PROCESSOR. Δ_e AND Δ_n, ARE ESTIMATED POSITION ERRORS IN THE EAST AND NORTH DIRECTION OF THE TRANSPONDERS. σ_r AND σ_a ARE STANDARD DEVIATIONS (IN METERS) OF ESTIMATION RESIDUALS IN RANGE AND AZIMUTH, DIVIDED INTO ERS SYSTEM NOISE (INDICES μ) AND ESTIMATION NOISE (INDICES n)

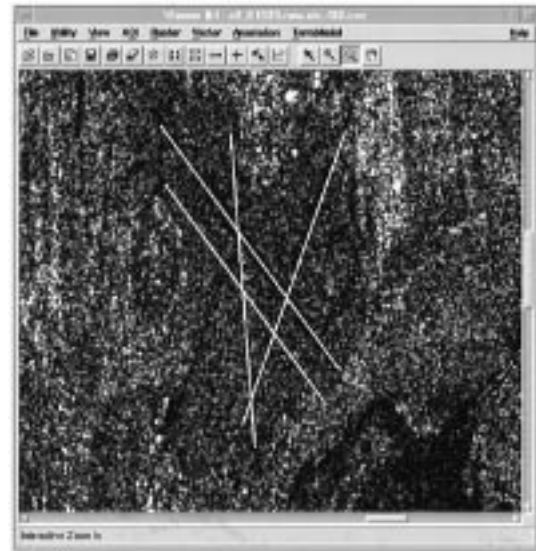| Flevoland calibration results			
	iter. 0	iter. 1	ESA
Δ_r	53.67	53.67	46.93
Δ_s	-9.94	-9.91	-9.25
Δ_e, T_1	6.39	-0.28	
Δ_n, T_1	53.37	-0.09	
Δ_e, T_2	-30.32	0.23	
Δ_n, T_2	-9.44	0.03	
Δ_e, T_3	-3.40	0.02	
Δ_n, T_3	-4.73	0.03	
$\sigma_{r,\mu}$	0.4	0.4	1.1
$\sigma_{r,n}$	0.4	0.4	2.1
$\sigma_{a,\mu}$	5.7	5.7	6.1
$\sigma_{a,n}$	0.3	0.3	1.9

Fig. 2. ERS image of Aalborg Airport, Denmark. The white lines are drawn on the runways.

TABLE IV
MEAN AND STANDARD DEVIATIONS OF PREDICTION ERRORS (IN METERS) FOR THE THREE INTERFEROGRAMS OVER THE VALIDATION SITE (AALBORG). INTERFEROGRAMS I1, I2, AND I3 ARE FORMED FROM THE TANDEM PAIRS WITH ERS-1 ORBITS 21 596, 23 099, AND 24 602, RESPECTIVELY

Validation on 5 runway crossings					
	I1	I2	I3	All	I2+I3
$\hat{\mu}_r$	0.8	3.3	0.2	1.4	1.7
$\hat{\sigma}_r$	1.9	2.0	4.0	3.0	3.4
$\hat{\mu}_a$	57.4	0.5	-8.4	-21.8	-4.0
$\hat{\sigma}_a$	2.9	6.2	10.3	27.1	9.3

is 1.7 m corresponding to 4.3 m on the ground, and the mean azimuth error is -4 m.

XI. VALIDATION (GREECE)

Corner reflectors with known 3-D positions are ideal for verification of the A/D sampling frequency f_s as compared to transponders, as they exhibit no potentially erroneous internal delay. By comparing the predicted pixel positions of the reflectors in near and far range of the slant range images, a shrink or stretch can be estimated. Such a shrink or stretch is directly proportional to A/D sampling frequency errors.

As part of the Framework IV Seismic Network Administration Program (SNAP) Project coordinated by the NPA Group, 6 large reflectors have been deployed in Corinth, Greece, and another six reflectors in Crete, Greece, [25]. The reflectors were surveyed with an accuracy on the order of 1 cm by using differential GPS [personal communication, Mark Haynes, NPA Group, Edenbridge, Kent, U.K.].

Here, we use ERS-1 images and ERS-2 images to assess the slant range difference between the expected and the observed positions (see Fig. 3). The figure shows no significant trends in the slant range errors. This confirms the validity of the D-PAF value for f_s. Also note that the slant range offset errors are within 3 m corresponding to 7 m on ground.

XII. LONG-TERM STABILITY

To assess the long term stability of the range offset and the along track timing calibration two time series of ERS images covering Death Valley, CA, were processed. The eleven-image ERS-1 time series was acquired between April 24, 1992 and November 7, 1999. The 15 image ERS-2 time series was acquired between September 25, 1995 and June, 21, 1999. For both series, a reference frame was selected and the remaining data aligned interferometrically with respect to that. The reference frames were acquired on September 24, 1995, and October 14, 1996 respectively. This approach is possible since many regions in the Death Valley area exhibit exceptionally good interferometric coherence (better than 0.8) even over a four year period.

The slant range and azimuth timing offsets are shown in Fig. 4. The figure indicates a ±3 m slant range offset drift for ERS-1. Although, this corresponds to ±7 m on ground, our approach has been to use data sets from 1995 to 1996 for slant range calibration and ignore the drift. No drift is seen for ERS-2.

With respect to azimuth timing drift, no clear evidence is seen in Fig. 4 for ERS-1 or ERS-2. One outlier is observed for the ERS-1 orbit 21 429 data acquired on August 20, 1995. The timewise coincidence with the two problematic frames (from Flevoland and Aalborg) in Fig. 1 strengthens our confidence that ERS-1 azimuth timing was somewhat degraded during the initial part of the Tandem phase.

XIII. STANDARD CALIBRATION DATA SET

For generation of SAR products with a good geometric fidelity, a SAR processor has to be calibrated (or verified) at least for slant range offset and azimuth timing errors.

We suggest to use the Flevoland site, covered by ascending orbit data from track 29, frame 1053, and by descending orbit
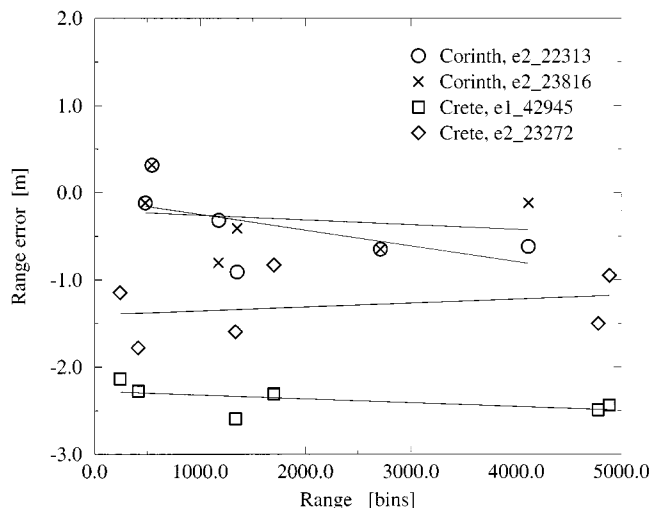

Fig. 3. Slant range offsets (in meters) for SNAP corner reflectors in Corinth and Crete, Greece. The thin lines are trend lines for each of the four frames.

(a)

(b)

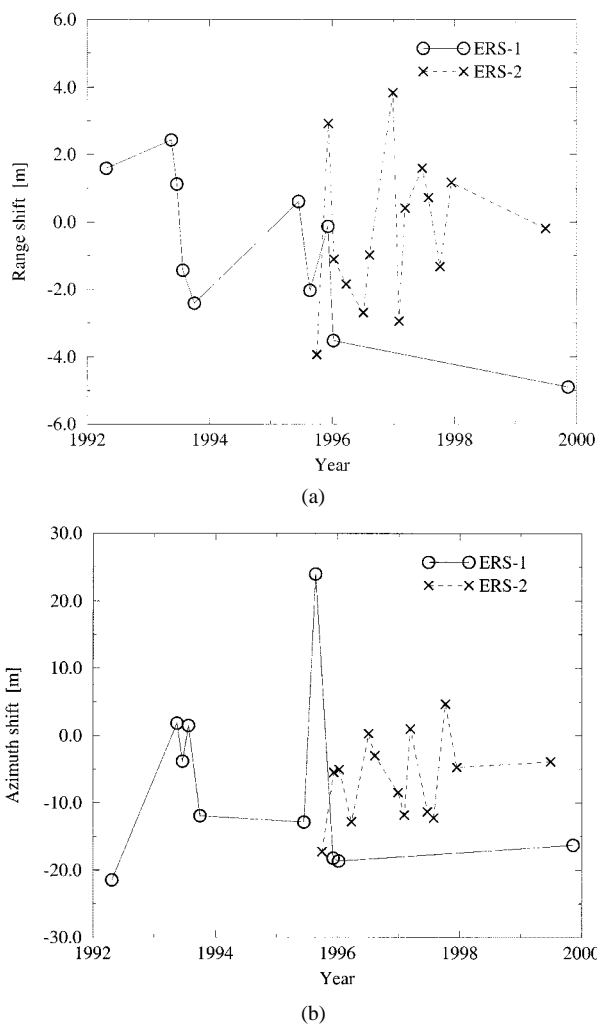Fig. 4. (a) Slant range and (b) azimuth offsets (in meters) required to align ERS images from Death Valley interferometrically. All data from track 399, frame 2878. Reference frames from ERS-1 orbit 21 930 and ERS-2 orbit 7768.

data from track 151, frame 2457. Good calibration pairs include the ascending orbit Tandem data set 25 067/05 394 and the descending orbit Tandem set 23 185/03 512. All three transponders

are operating in all four images and in our calibration experiment, the along-track errors are closest to the mean value for those pairs.

At present, we believe that the most accurate estimate of the transponder positions are those estimated from ERS data [see Table II, (ϕ_E, λ_E)]. However, ESA plans to resurvey the transponders in preparation for the ENVISAT ASAR.

XIV. Conclusions

A simple algorithm for extraction of SAR parameters and a method for raw data preparation is provided. It is demonstrated that by using the outlined dead-reckoning method, a relation between the SAR geometry (slant range, squint angle) and a geographical system can be established with a 10 m horizontal accuracy.

The accuracy of the results has been verified by using ERS imagery from one American and three European sites. Both passive and active reference targets were used. Also, the long term drift of the ERS system, including both hardware and data annotation procedures, has been assessed and no significant drift was found, although a minor range drift was observed for ERS-1.

The results demonstrate the high stability of the ERS satellites, the systems for controlling the satellites, the estimation of orbit state-vectors, and the on-ground processing chain.

The excellent geometric properties of ERS data are of great value for exploitation of ERS data. On the one hand, it simplifies SAR processing, interferometric SAR processing, and geocoding, as dead-reckoning methods can be used. On the other hand, it broadens the application field, since accurate geocoding is crucial for many applications but difficult or even impossible due to lack of ground control points.

APPENDIX I
RAW SAR IMAGE DATA PROCECESSING

The ERS.SAR.RAW data used, provided in CEOS format by ESA, will be denoted the RAW product, [18]. The RAW product consists of four files but only the Leader File and the Data Set File with the actual SAR data are relevant here. Table V summarizes the important parameters which are provided in the auxiliary information of each raw data line.

A. Missing Line Cleaning Algorithm

The developed algorithm relies on the assumptions that the order of lines is always correct, and bit-errors in the IFC are not systematic.

The overall algorithm works as follows. The lines are read one line at a time. As long as the IFC is correct (k lines with consecutive IFC values), the lines are output to the file. If the IFC values are not consecutive, the lines are read and queued until k lines with consecutive IFC values are found. If the number of lines in the queue matches the number expected, the IFC values are corrected and all lines in the queue output. If the number of lines in the queue does not match the expected, all but k lines in the queue are discarded and an appropriate number of dummy lines added. We have used $k = 3$ successfully until now. An implementation of the algorithm is outlined in [26].

TABLE V
IMPORTANT PARAMETERS FOR EACH RAW DATA LINE. PARENTHESES INDICATE THAT THE ACTUAL VALUE OF THAT PARAMETER IS NOT USED BY US BUT IS FIXED IN OUR PROCESSING SCHEME

Signal Data Record (data set file)		
Bytes	Symbol	Description
205–208	ICU	on board time
211–214	IFC	image format counter
215–216	SWST	sampling window start time
217–218	(PRI)	pulse repetition interval

This algorithm also handles bit errors in the beginning and end of the file in a robust manner. In that case, faulty lines will be queued but never output, because they are not enclosed by blocks of k consecutive IFC values.

B. SWST Cleaning Algorithm

We have chosen a simple algorithm. First, we select a desired SWST value for the cleaned data. The desired SWST can either be set automatically by searching for the first three consecutive lines with identical SWST values or set manually.

The SWST of each line is bit cleaned separately. Only SWST values differing from the desired SWST by a multiple of 22 units are considered valid. If a nonvalid SWST is encountered it is set to the value of the previous line.

If the SWST of the first line is not a valid SWST, it is not changed. This nonvalid SWST value can thus ripple from the start line to the first line encountered with a valid SWST.

Following the bit cleaning, each line is shifted in accordance with the desired SWST. The length of the lines can simultaneously be changed to avoid any loss of data.

C. ICU Estimation Algorithm

The ICU values are provided in each raw data line header (see Table V). Since one ICU step corresponds to 1/256 s and updated every fourth pulse, the accuracy is too coarse for high precision geocoding. In this section, a method for calculating a floating point ICU using many radar lines is devised. In the selected estimation scheme, a new $(n_{\text{raw}} - 2, \text{ICU})$ pair is stored in a buffer each time the ICU increases by exactly one. The logic is that every time the ICU is updated the transition took place between zero and four pulses earlier. When 1000 points are stored, a line is fitted. Since only ICU steps by exactly one are considered, ICU values with bit errors are in effect discarded.

APPENDIX II
AUXILIARY DATA PROCESSING

Tables V and VI summarize the parameters used from the signal data record (SDR) of the raw data file and the data set summary record (DSS) of the leader file. The following sections describe how the required parameters are derived.

A. Sampling Frequency f_s

The sampling frequency used is

$$f_s = 18.962\,468 \text{ MHz}.$$

TABLE VI
IMPORTANT PARAMETERS FROM THE LEADER FILE. PARENTHESES INDICATES
THAT THE ACTUAL VALUE OF THE PARAMETER IS FIXED IN OUR PROPOSED
PARAMETER EXTRACTION SCHEME

Data Set Summary Record (leader file)		
Field	Symbol	Description
41	(f_c)	carrier frequency
52	(c_2)	chirp phase coef. (quadratic)
57	(f_s)	sampling frequency
59	(T_p)	pulse length
77	ICU_b	satellite binary time
78	ICU_t	satellite clock time (UTC)
79	(ICU_Δ)	satellite clock step (1/256 s)

The value has not been consistent in the leader files processed by us. The value presented above is the one provided by the D-PAF. Compared to the commonly cited value of 18.96 MHz, it represents shrinking the ground swath width by 15 m. Compared to the value of 18.962 431 MHz derived by doubling of a reference oscillator frequency of 61.6279 MHz, followed by a division by 13 and a multiplication by 2, it represents shrinking the ground swath width by 20 cm, (i.e., 7 cm in slant range).

The analysis of pixel positions of corner reflectors in near and far range of the images does not have sufficient accuracy to distinguish a 7 cm slant swath shrink, corresponding to less than 1/100 of the range pixel spacing, see Section XI. For most, if not all, applications, it is also insignificant. The corner reflector analysis, though, does confirm that the selected value of f_s is sufficiently accurate.

From the selected value of f_s, a value for $4T_s = 4/f_s = 210.943\,006$ ns is found, where T_s is the sampling interval. The values of other parameters e.g., the pulse repetition interval, are based on $4T_s$.

It is also noted that the above mentioned choice of f_s makes the ICU timer (which time-tags the radar lines) consistent with A/D sampling timing. It is not evident that it should be so, since the two clocks are independent. It adds to our confidence in the above quoted value for f_s that the pulse repetition period derived in the next section using this value of f_s is consistent with long time averages derived from UTC and the ICU counter. From 37 ERS-1/2 frames we estimated the slope of the ICU to be $\text{ICU}_{\text{slope}} = 0.152\,392\,052$, which combined with the ICU_Δ value of 1/256 s from the leader file gives $T_p = 0.595\,281\,456$ ms. This is in good agreement with the value of T_p calculated below by using the A/D sampling frequency f_s.

B. Pulse Repetition Interval T_p

The pulse repetition interval is derived from

$$T_p = 4T_s\,(\text{PRI} + 2).$$

The integer PRI value is fixed for every phase of ERS-1 and ERS-2, (personal communication, ERS Helpdesk). For ERS-1 phase G and ERS-2 phase A, i.e., the entire ERS-2 mission at least including August 2000, PRI=2820, corresponding to $T_p = 0.595\,281\,163$ ms. The resulting PRF of $1/T_p$ differs from the nominal PRF value in the leader file by -0.02 Hz, corresponding to an along track stretch of 12 m over a 1000 km strip.

It is also noted that the alternative value $f_s = 18.962\,431$ MHz discussed above, represents a 2 m along track stretch over a 1000 km strip. This is 1/15 of a pixel assuming an 8 pixel azimuth averaging, which is typically used in ERS imagery.

C. Slant Range Offset t_0

The slant range offset is derived from

$$t_0 = 9T_p + \text{SWST} \cdot 4T_s - t_{0,b} + t_{0,s}$$

where $t_{0,b}$ is a common slant range bias and $t_{0,s}$ the bias difference between ERS-1 and ERS-2. The selected values of T_p and $4T_s$ are provided above. We have determined the common bias to be $t_{0,b} = 6.622\ \mu s$ from calibration experiments using Flevoland data, see Section IX. It includes both the actual bias, shifts relating to our specific implementation of the range compression using a nominal linear FM chirp, and an atmospheric bias. Interferometric processing of many data sets also shows a systematic difference between the ERS-1 and ERS-2 slant range offsets, see Section VII. We define $t_{0,s} = 0$ s for ERS-1 and find $t_{0,s} \approx -0.025\ \mu s$, corresponding to -3.75 m, for ERS-2, see Section VII.

D. Time Of First Line t_l

The time of first line is derived from

$$t_l = (t_{l,0} - \text{ICU}_b) \cdot \text{ICU}_\Delta + \text{ICU}_t + t_{l,b}$$

where $t_{l,0}$ is the estimated ICU of first line (see Appendix A), $\text{ICU}_\Delta = 1/256$ s, ICU_b and ICU_t extracted from the leader file (see Table VI), and the along track bias $t_{l,b} = 1.25$ ms found from our Flevoland calibration experiment (see Section IX).

E. Carrier Frequency f_c

The carrier frequency used is

$$f_c = 5.300\ \text{GHz}.$$

Though consistent in all leader files processed by us until now, we have chosen to fix it. The value is consistent with a carrier frequency of 5.300 010 GHz derived by frequency division and multiplication of f_s.

F. Chirp Length T_c

The chirp length used is

$$T_c = 37.12\ \mu s.$$

G. Chirp Bandwidth B_c

The chirp bandwidth used is

$$B_c = 15.508\,29\ \text{MHz}.$$

process. They would also like to thank P. Meadows, GEC-Marconi, Essex, U.K., for files with transponder activity versus orbit numbers, and H. Jackson, ESA/ESTEC, Noordwijk, the Netherlands, and N. Wiik, ESA/ESRIN, Frascati, Italy, for information regarding the characteristics and positions of the transponders in Flevoland. They also wish to thank R. Gelsthorpe, ESA/ESTEC, for information on the frequency scheme of the ERS-1/2 radars and M. Haynes, NPA Group, Edenbridge, Kent, U.K., for sharing with them the positions of the 12 corner reflectors deployed in Greece in the framework of the SNAP project.

REFERENCES

[1] P. J. Meadows, H. Laur, and B. Schättler, "The calibration of ERS SAR imagery for land applications," *Earth Observ. Quart.*, no. 62, pp. 5–8, 1999.

[2] H. Laur, P. Bally, P. Meadows, J. Sánchez, B. Schättler, E. Lopinto, and D. Esteban, "ERS SAR calibration: Derivation of the backscattering coefficient sigma-nought ESA ERS SAR PRI products," Tech. Rep. ES-TN-RS-PM-HL09, Rev. 5b, European Space Agency (ESA)/ESRIN, Ispra, Italy, Sept. 1998.

[3] S. Nørvang Madsen and H. Zebker, "Imaging radar interferometry," in *Manual of Remote Sensing*, 3rd ed, F. M. Henderson and A. J. Lewis, Eds. New York: Wiley, 1998, vol. 2, ch. 6, pp. 359–380.

[4] R. Bamler and P. Hartl, "Synthetic aperture radar interferometry," *Inv. Probl.*, vol. 14, pp. R1–R54, 1998.

[5] D. Massonnet and K. L. Feigl, "Radar interferometry and its application to changes in the Earth's surface," *Rev. Geophys.*, vol. 36, pp. 441–500, Nov. 1998.

[6] P. A. Rosen, S. Hensley, I. R. Joughin, F. Li, M. S. N. E. Rodriguez, and R. M. Goldstein, "Synthetic aperture radar interferometry," *Proc. IEEE*, vol. 88, pp. 333–382, Mar. 2000.

[7] J. J. Mohr, S. Nørvang Madsen, and N. Reeh, "ERS tandem study of glacier dynamics in NE-Greenland," in *Proc. 3rd ERS Symp.: Space at the Service of our Environment*, Florence, Italy, Mar. 1997, pp. 989–993.

[8] R. Bamler, "A comparison of range-doppler and wavenumber domain SAR focussing algorithms," *IEEE Trans. Geosci. Remote Sensing*, vol. 30, pp. 706–713, July 1992.

[9] J. C. Curlander, "Location of spaceborne SAR imagery," *IEEE Trans. Geosci. Remote Sensing*, vol. GE-20, pp. 359–364, May 1982.

[10] T. Gruber, F.-H. Massmann, and C. Reigber, "ERS D-PAF altimeter and orbit global products manual," Tech. Rep. ERS-D-GPM-31200, GFZ/D-PAF, Oberpfaffenhofen, Germany, Dec. 1996.

[11] S. Y. Zhu, C. Reigber, and F.-H. Massmann, "ERS standards used at D-PAF: The German PAF for ERS," Tech. Rep. ERS-D-STD-31 101 Rev. B, GFZ/D-PAF, Oberpfaffenhofen, Germany, Sept. 1996.

[12] F.-H. Massmann, J. C. Neumayer, K. Raimondo, K. Enninghorst, and H. Li, "Quality of the D-PAF orbits before and after the inclusion of PRARE data," in *Proc. 3rd ERS Symp.: Space at the Service of our Environment*, vol. 3, Florence, Italy, Mar. 1997, pp. 1655–1660.

[13] R. Zandbergen, "ERS operational vs. precise orbit comparison," European Space Operations Centre, Darmstadt, Germany, http://nng.esoc.esa.de/ers/ocompo.html.

[14] R. Zandbergen, F. Martinez Fadrique, M. Romay Merino, and R. Piriz, "Progress in ERS orbit and tracking data analysis," in *Proc. 3rd ERS Symp.: Space at the Service of Our Environment*, Florence, Italy, Mar. 1997, pp. 1669–1679.

[15] Earth Observation Mission Support Division (JW) ESTEC and DORNIER System Team, "ERS-1 satellite to ground segment interface specification," Tech. Rep. ER-IS-ESA-GS-0001, ESA, Nordwiijk, The Netherlands, Sept. 1993.

[16] J. Louet, "ERS-1 operation capabilities," in *Proc. IGARSS'88*, Edinburgh, U.K., Sept. 1988, pp. 855–858.

[17] R. Francis *et al.*, "The ERS-1 spacecraft and its payload," in *ERS-1 Special Issue*. Noordwijk, The Netherlands: ESA, Feb. 1991, pp. 26–48.

[18] O. Gråbak, "Annex A, ERS SAR.RAW, CCT and EXABYTE," Tech. Rep. ER-IS-EPO-GS-5902.1, ESA, Noordwijk, The Netherlands, Dec. 1995.

[19] ESA, "Announcement of opportunity for ERS-1, technical annex: ERS-1 system description," in *Proposal Material*. Noordwijk, The Netherlands: ESA, 1996.

[20] M. Eineder, B. Schättler, M. Hubig, W. Knöpfle, N. Adam, and H. Breit, "Operational processing large areas of interferometric SAR data," Available on CD-ROM: Advancing ERS SAR Interferometry from Applications towards Operations, ESA, Noordwijk, The Netherlands, 1999.

[21] H. D. Jackson and A. Woode, "Development of the ERS-1 active radar calibration unit," *IEEE Trans. Microwave Theory Tech.*, vol. 40, pp. 1063–1069, Nov. 1992.

[22] A. Woode, Y.-L. Desnos, and H. D. Jackson, "The development and first results from the ESTEC ERS-1 active radar calibration unit," *IEEE Trans. Geosci. Remote Sensing*, vol. 30, pp. 1122–1130, Nov. 1992.

[23] E. Topografische Dienst, "Netherland 1:50000, sheets: 20 Oost Lelystad (1995), 25 Oost Amsterdam (1998), 26 Oost Harderwijk (1999),".

[24] "The Danish national survey and cadastre 1:25 000 (4 cm), sheet: 1217 II S0 GJ0L," Danish National Survey, Copenhagen, Denmark, 1989.

[25] M. Haynes, "Corner reflector aspects of the SNAP program: Demonstrating the utility of differential SAR interferometry for the assessment of earthquake risk," Available on CD-ROM: Advancing ERS SAR Interferometry from Applications towards Operations, ESA, Noordwijk, The Netherlands, 1999.

[26] J. J. Mohr and S. Nørvang, "Automatic generation of large scale ERS DEM's and displacement maps," Available on CD-ROM: Advancing ERS SAR Interferometry from Applications towards Operations, ESA, Noordwijk, The Netherlands, 1999.

Johan Jacob Mohr received the M.Sc.E.E. and Ph.D. degrees from the Technical University of Denmark (TUD), Lyngby, in 1992 and 1997, respectively.

Since then, he has been working as Research Assistant Professor with the Danish Center for Remote Sensing, TUD. His main interests are methods and principles relating to satellite and airborne SAR interferometry particularly as applied to glaciological studies.

Søren Nørvang Madsen (S'83–M'84) received the M.Sc.E.E. and Ph.D. degrees from the Technical University of Denmark (TUD), Lyngby, in 1982 and 1987, respectively.

He has been with the Electromagnetics Institute, now Department of Electromagnetic Systems (EMI), TUD, since 1982. His work has included all aspects of synthetic aperture radar (SAR), including development of preprocessors, analysis of basic properties of SAR images, postprocessing, and SAR systems design. From 1987 to 1989, he was an Associate Professor with EMI, working on the design of radar systems for mapping the earth and other planets as well as the application of digital signal processing systems in radar systems. He initiated and lead the Danish Airborne SAR program from its start until he left EMI in 1990 to join NASA's Jet Propulsion Laboratory (JPL), Pasadena, CA, where he worked on geolocating SEASAT and SIR-B SAR data and led the development of a SIR-C calibration processor prototype. He was involved in the Magellan Venus radar mapper project. Since 1992, his main interest has been interferometric SAR systems. He led the development of the processing systems for the JPL/NASA across-track interferometer (TOPSAR) as well as the ERIM IFSAR system. From 1993 to 1996, he split his time between JPL and EMI. During that time, his JPL work included the development of processing algorithms for ultra wide-band UHF SAR systems. At EMI, he was a Research Professor from 1993 to 1998, when he became a Full Professor. He has headed the Danish Center for Remote Sensing (DCRS) since its start in 1994. His work covers all aspects relating to the airborne Danish dual-frequency polarimetric and interferometric SAR. At DCRS, he is also a Principal Investigator for two ERS-1/2 satellite SAR studies.